FRONTIERS OF PHYSICS

RESEARCH ARTICLE
Volume 19 / Issue 2 / 23203 / 2024

# Magnetic phase transition and continuous spin switching in a high-entropy orthoferrite single crystal

Wanting Yang[1,2], Shuang Zhu[1], Xiong Luo[3], Xiaoxuan Ma[1,2], Chenfei Shi[1], Huan Song[1], Zhiqiang Sun[1], Yefei Guo[1], Yuriy Dedkov[1], Baojuan Kang[1,2], Jin-Ke Bao[1], Shixun Cao[1,2,4,†]

1 Department of Physics, Shanghai University, Shanghai 200444, China
2 Materials Genome Institute and International Center for Quantum and Molecular Structures, Shanghai University, Shanghai 200444, China
3 School of Physics, Southeast University, Nanjing 211189, China
4 Shanghai Key Laboratory of High Temperature Superconductors, Shanghai University, Shanghai 200444, China
Corresponding author. E-mail: †sxcao@shu.edu.cn

Received June 6, 2023; accepted August 28, 2023

## ABSTRACT

Rare-earth orthoferrite $RE\mathrm{FeO}_3$ (where $RE$ is a rare-earth ion) is gaining interest. We created a high-entropy orthoferrite $(\mathrm{Tm}_{0.2}\mathrm{Nd}_{0.2}\mathrm{Dy}_{0.2}\mathrm{Y}_{0.2}\mathrm{Yb}_{0.2})\mathrm{FeO}_3$ (HEOR) by doping five $RE$ ions in equimolar ratios and grew the single crystal by optical floating zone method. It strongly tends to form a single-phase structure stabilized by high configurational entropy. In the low-temperature region (11.6–14.4 K), the spin reorientation transition (SRT) of $\Gamma_2$ ($F_x$, $C_y$, $G_z$)–$\Gamma_{24}$–$\Gamma_4$ ($G_x$, $A_y$, $F_z$) occurs. The weak ferromagnetic (FM) moment, which comes from the Fe sublattices distortion, rotates from the *a*- to *c*-axis. The two-step dynamic processes ($\Gamma_2$–$\Gamma_{24}$–$\Gamma_4$) are identified by AC susceptibility measurements. SRT in HEOR can be tuned in the range of 50–60000 Oe, which is an order of magnitude larger than that of orthoferrites in the peer system, making it a candidate for high-field spin sensing. Typical spin-switching (SSW) and continuous spin-switching (CSSW) effects occur under low magnetic fields due to the strong interactions between $RE$– Fe sublattices. The CSSW effect is tunable between 20–50 Oe, and hence, HEOR potentially can be applied to spin modulation devices. Furthermore, because of the strong anisotropy of magnetic entropy change ($-\Delta S_\mathrm{m}$) and refrigeration capacity (*RC*) based on its high configurational entropy, HEOR is expected to provide a novel approach for refrigeration by altering the orientations of the crystallographic axes (anisotropic configurational entropy).

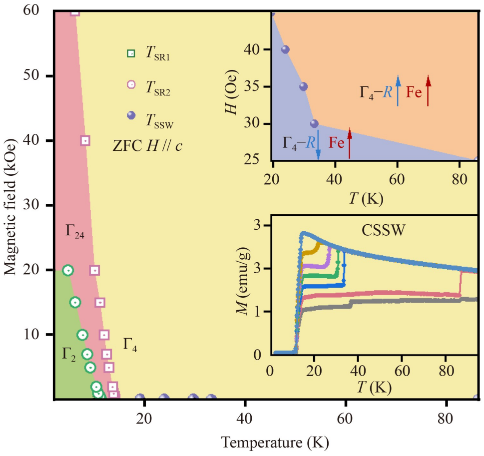

**Keywords** high-entropy oxide, rare-earth orthoferrite, spin reorientation transition, spin switching, magnetocaloric effect

## 1 Introduction

There are plenty of magnetic properties caused by specific crystal and magnetic structures [1, 2] in rare-earth orthoferrite $RE\mathrm{FeO}_3$ (where $RE$ is a rare-earth element). $RE\mathrm{FeO}_3$ usually belongs to the orthorhombic system and has a distorted perovskite structure with the *Pbnm* space group [3]. The tolerance factor $\tau$ implies the

Higher Education Press

https://doi.org/10.1007/s11467-023-1343-x

degree of distortion:

$$\tau = \frac{R_{RE} + R_{\text{O}}}{\sqrt{R_{\text{Fe}} + R_{\text{O}}}}, \tag{1}$$

where $R_{RE}$, $R_{\text{Fe}}$, and $R_{\text{O}}$ represent the ionic radii of $RE$, Fe, and O sites [4]. Since the majority of $RE$ and Fe ions are magnetic, there are three interactions between $RE$ and Fe sublattices: $RE$–$RE$, $RE$–Fe, and Fe–Fe interactions [5, 6]. At the Néel temperature $T_{\text{N1}}$ (650–750 K), Fe–Fe interactions cause the Fe sublattices' transition from a canted antiferromagnetic (AFM) to a paramagnetic (PM) state. The canted AFM state refers to the non-strictly antiparallel alignment of Fe ion moment caused by the Dzyaloshinsky–Moriya (D–M) interaction [5, 7]. Thus, there is a weak ferromagnetic (FM) moment along the easy-axis in orthoferrites. The $RE$FeO$_3$ unit cell contains 4 Fe ions, each with a magnetic moment of $m_1$, $m_2$, $m_3$, and $m_4$, respectively. Therefore, the weak FM moment ($F$) and $A$-, $C$- and $G$-type AFM moment can be expressed as

$$F = m_1 + m_2 + m_3 + m_4,\ A = m_1 - m_2 - m_3 + m_4,$$
$$C = m_1 + m_2 - m_3 - m_4,\ G = m_1 - m_2 + m_3 - m_4. \tag{2}$$

Using Bertaut's notation, the configuration and the net moment associated with it are identified as $\Gamma_1$ ($A_x$, $G_y$, $C_z$), $\Gamma_2$ ($F_x$, $C_y$, $G_z$), $\Gamma_4$ ($G_x$, $A_y$, $F_z$) [8, 9]. The rotation of the Fe sublattices net moment from one axis of symmetry to another is known as spin reorientation transition (SRT) [10, 11]. Typically, SRTs are classified into two types upon cooling: $\Gamma_4$–$\Gamma_2$ [12–16] and $\Gamma_4$–$\Gamma_1$ [17, 18]. The magnetic ordering temperature of $RE$ sublattices $T_{\text{N2}}$ is generally lower, at 2–10 K. Yet, some of the $RE$ sublattices will be magnetized by the molecular field of ordered Fe sublattices above $T_{\text{N2}}$, resulting in a net moment. Because of the $RE$–Fe interactions, magnetic sublattices may undergo a spin flip called the spin-switching (SSW) effect. The type-I SSW effect occurs when $RE$ and Fe sublattices spin flip simultaneously [19–21], while the type-II SSW occurs if only the $RE$ sublattice spin flip [15, 18].

$RE$FeO$_3$ has lately attracted interest as a novel series of materials of magnetocaloric effect (MCE) [22–24]. The temperature decreases when a magnet is magnetized by an external field through the adiabatic process [25]. MCE-based magnetic refrigeration can replace conventional gas compression or expansion method. And, magnetocrystalline anisotropy has been reported to be directly applicable to refrigeration in $RE$FeO$_3$, $RE$MnO$_3$, and $RE$Mn$_2$O$_5$ [22, 26, 27]. High-entropy alloy (HEA) has drawn increasing attention since the first proposal by Yeh *et al.* in 2004 [28]. And the high-entropy oxide $A_xB_y\text{O}_z$ (HEO) developed from HEA provides ideas and guidance for the development of new material systems [29–31]. The definition is a single-phase oxide solid solution containing five or more elements in an equal or close to equal atomic ratio at $A$ or $B$ site, and the term "entropy" refers to the mixing entropy. The configurational entropy of HEO can be computed using the formula (3) and if the contribution of particles at $B$ and O sites to the configurational entropy is ignored, it can be simplified to the formula (4) [32]:

$$S_{\text{config}} = -R\left[x\left(\sum_{a=1}^{M} x_a \ln x_a\right)_{a\text{-site}} + y\left(\sum_{b=1}^{M} y_b \ln y_b\right)_{b\text{-site}} + z\left(\sum_{c=1}^{M} z_c \ln z_c\right)_{c\text{-site}}\right], \tag{3}$$

$$S_{\text{config}} = -R\left[x\left(\sum_{a=1}^{M} x_a \ln x_a\right)_{a\text{-site}}\right], \tag{4}$$

where $x_a$, $x_b$, $x_c$ is the mole fraction of particles at $A$, $B$, and $C$ sites, and $R$ is the gas constant [the value is 8.314 J/(mol·K)]. The configurational entropy of a multi-component system is higher when the amount of moles of each cation is identical. When the number of components $N = 5$ and the moles of each component are equal, $S_{\text{config}} = 1.61\ R$ [29]. The large configurational entropy of HEO lowers the free energy to increase system stability.

We combined the concept of orthoferrite $RE$FeO$_3$ and HEO to create a high-entropy orthoferrite (Tm$_{0.2}$Nd$_{0.2}$Dy$_{0.2}$Y$_{0.2}$Yb$_{0.2}$)FeO$_3$ (HEOR). Intriguing magnetic characteristics are obtained by the high-entropy design. The tunable SRT occurs, proving that the interactions of Fe–Fe sublattices can be impacted by both temperature and magnetic field. The typical and tunable continuous SSW effects indicate that the $RE$–Fe interactions can also be affected by physical fields. By measuring AC susceptibility, the dynamic process of the SRT is determined. Fe sublattices undergo two-step transitions from $\Gamma_2$ to $\Gamma_{24}$ and then to $\Gamma_4$. Also, HEOR has a considerable magnetic entropy anisotropy and an excellent magnetic refrigeration capacity based on the high configurational entropy. So, it can be used for spintronic and magnetic refrigeration applications.

## 2 Experimental details

HEOR single crystal with high quality was grown by the optical floating zone method (see Appendix A). A powder X-ray diffraction (XRD) pattern was collected on a diffractometer with monochromatic copper K$_\alpha$ radiation (Bruker D2 PHASER) to examine the phase purity. Crystallographic orientations were achieved using a back reflection Laue X-ray diffractometer with a tungsten target (Try-SE. Co., Ltd.). The crystallographic orientations were confirmed by XRD after cutting it into

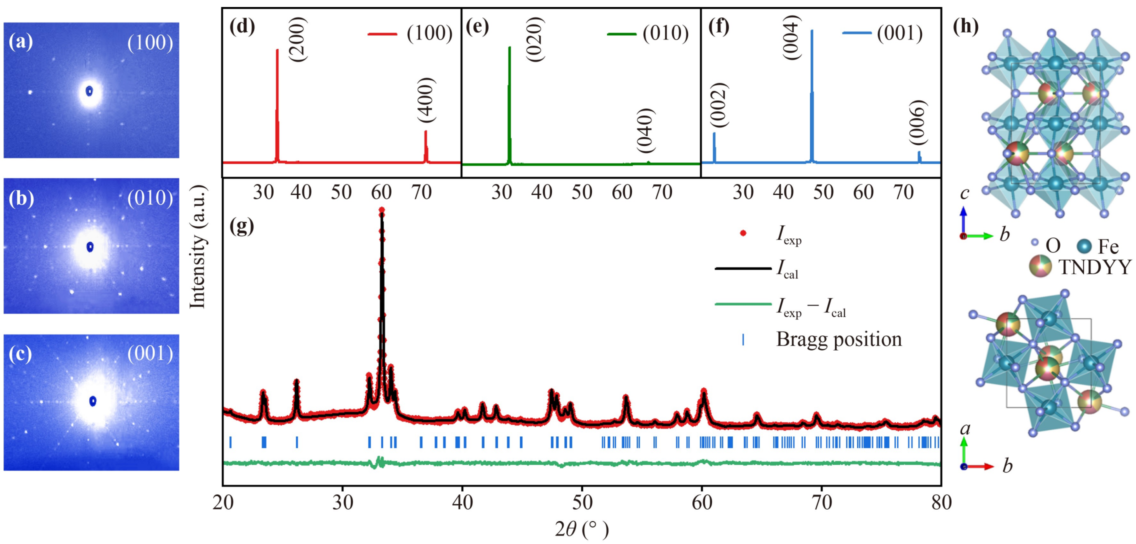

**Fig. 1** **(a–c)** The Laue diffraction spectra along the *a*-, *b*-, and *c*-axes; **(d–f)** the XRD spectra along the *a*-, *b*-, and *c*-axes. **(g)** Powder XRD spectrum of HEOR single crystal, Rietveld refinement diagram obtained by FullProf Suite. **(h)** The crystal structure of HEOR from different viewing, and the structure data gotten by Rietveld refinement. The purple, green, and colored balls represent oxygen, iron, and the five rare-earth atoms at the *RE* site, respectively.

a cube. The high-resolution energy-dispersive-spectroscopy (EDS) mapping of *RE* elements was performed by field emission scanning electron microscopy (SEM) (Hitachi FlexSEM1000). Magnetization was measured utilizing a Physical Property Measurement System (PPMS-14T, Quantum Design Inc.) with a Vibrating Sample Magnetometer (VSM) option. The temperature dependences of the magnetization were obtained in the zero-field-cooling (ZFC), field-cooled-cooling (FCC), as well as field-cooled-warming (FCW) modes.

For X-ray photoelectron spectroscopy (XPS) experiments the HEOR sample was mounted on Mo sample holders and then were annealed under ultra-high vacuum (UHV) conditions at 600 °C for 30 min and sputtered by using $\mathrm{Ar}^+$ for 15 mins (under $1.5 \times 10^{-5}$ mbar, 1.5 keV, and 10 mA conditions). Temperature of the sample was measured using calibrated pyrometer. Laboratory-based XPS experiments were performed in UHV station installed at Shanghai University and consisting of preparation and analysis chambers with a base pressure better than $1 \times 10^{-10}$ mbar (SPECS Surface Nano Analysis GmbH). XPS spectra were measured using a monochromatized Al Kα ($h\nu$ = 1486.6 eV) X-ray source and SPECS PHOIBOS 150 hemispherical analyzer combined with a 2D-CMOS detector.

## 3 Results and discussion

### 3.1 Structural characterization

The Laue back reflection XRD was performed to determine the crystallographic axes. The distinct Laue diffraction patterns demonstrate the high quality of HEOR as illustrated in Figs. 1(a)–(c). XRD was conducted on a slice of crystal face to confirm the crystallographic orientation found in the Laue photograph. The XRD patterns with $\theta$–$2\theta$ scanning of the cutting plane are displayed in Figs. 1(d)–(f). The peaks can be donated by ($h$00), (0$k$0), or (00$l$) ($h$, $k$ = 2, 4, and $l$ = 2, 4, 6). Thus, the cut plane was precisely perpendicular to the *a*-, *b*-, and *c*-axes, respectively, according to both XRD and Laue photography. The powder XRD spectrum [see Fig. 1(g)] with no impurity or orientation faults indicates the high quality and high homogeneity degree of the HEOR single crystal. The lattice parameters $a$ = 5.3030 Å, $b$ = 5.5917 Å, and $c$ = 7.6310 Å are obtained from Rietveld refinement. The lattice parameters and Fe–O bonding lengths are also obtained and shown in Table 1. The crystal structure was created using Vesta software, as shown in Fig. 1(h), and it features a distorted perovskite structure with a space group of *Pbnm*.

Survey XPS spectrum of the HEOR sample is presented in Fig. 2, the contaminated carbon and adsorbed oxygen were removed after the annealing and $\mathrm{Ar}^+$ sputtering treatment, indicating the presence of Tm, Nd, Dy, Y, Yb, Fe, and O elements. The peak located at 530.3 eV is assigned to the O 1*s*, 709 and 721.5 eV are corresponding to Fe 2*p*, 124.7 and 178 eV correspond to Tm 4*d*, 984.5 and 1006.5 eV to Nd 3*d*, 1299.0 and 1336.5 eV to Dy 3*d*, 158.9 and 190.8 eV to Y 4*d*, and 186.6 eV to Yb 4*d*. We quantitatively analyzed the elements of the full spectrum with atomic percentages of 60.350% (O), 20.111% (Fe), 3.931% (Tm), 3.937% (Nd), 3.963% (Dy), 3.908% (Y), and 3.900% (Yb). The atomic ratio of the *RE* site elements Tm:Nd:Dy:Y:Yb is 1:1.00: 1.01:0.99:0.99, which fits the definition of HEO. The

**Table 1** Lattice constants, crystal volume, and Fe–O bonding lengths of HEOR single crystal and the parents. Data of HEOR was gotten by the results of XRD Rietveld analysis.

| | $TmFeO_3$ | $NdFeO_3$ | $DyFeO_3$ | $YFeO_3$ | $YbFeO_3$ | HEOR |
|---|---|---|---|---|---|---|
| $a$ (Å) | 5.2510 | 5.4489 | 5.3009 | 5.2743 | 5.2330 | 5.3030 |
| $b$ (Å) | 5.5760 | 5.5887 | 5.5957 | 5.5877 | 5.5570 | 5.5920 |
| $c$ (Å) | 7.5840 | 7.7619 | 7.6290 | 7.5951 | 7.5700 | 7.6310 |
| Cell volume (Å$^3$) | 222.0563 | 236.3675 | 226.2933 | 223.8368 | 220.1339 | 226.2925 |
| Fe–O1 (Å) | 2.0047 | 2.0015 | 2.0024 | 1.9984 | 2.0055 | 2.0035 |
| Fe–O2 (Å) | 2.0265 | 2.0211 | 2.0250 | 2.0273 | 2.0257 | 2.0869 |
| Fe–O3 (Å) | 2.0025 | 2.0083 | 2.0120 | 2.0033 | 2.0008 | 1.9260 |

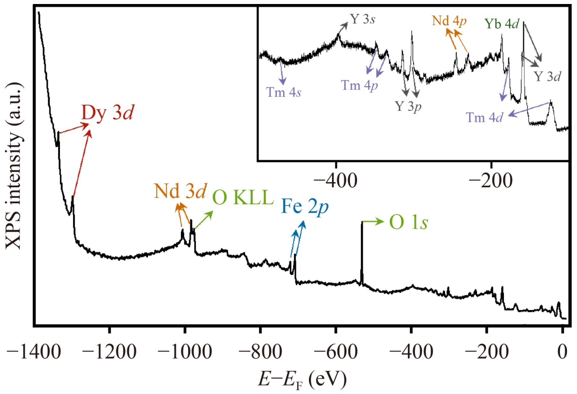

**Fig. 2** XPS survey scans for annealed and sputtered HEOR. The inset shows a zoomed-in view of the spectrum from –500 to –100 eV.

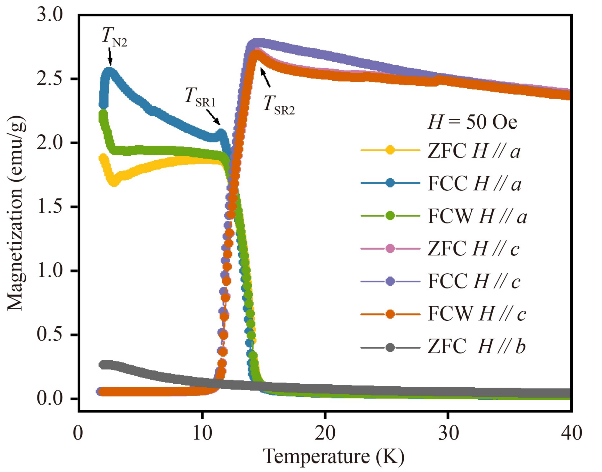

**Fig. 3** Temperature dependences of the magnetization curves along the $a$-, $b$-, and $c$-axes at 50 Oe.

result of EDS mappings (Fig. A2) is consistent with the XPS spectrum and proves the isoproportionality of the HEOR $RE$-site elements. The atomic ratio of the $RE$, Fe, and O sites is 1:1.03:3.08, indicating that HEOR composition is in accordance with the $RE$$FeO_3$ definition of 1:1:3.

### 3.2 Magnetic characterization

Under a magnetic field of 50 Oe, the $M$–$T$ curves were measured (Fig. 3). The strong magnetic anisotropy originating from Fe and $RE$ sublattices spin–orbit coupling is one of the key characteristics of HEOR, which leads to strikingly distinct temperature dependences of $M_a$, $M_b$, and $M_c$. In ZFC mode, the initial magnetization along the $a$-axis is 1.86 emu/g and that along the $b$- and $c$-axes are approximately zero at 2 K, indicating that the Fe sublattices are in the spin configuration $\Gamma_2$ ($F_x$, $C_y$, $G_z$). The magnetic characteristics are dominated by both $RE$ and Fe sublattices in the low-temperature region. With the temperature increasing, the interactions weaken, and the total magnetization increases. As the temperature rises from $T_{\mathrm{SR1}} = 11.6$ K to $T_{\mathrm{SR2}} = 14.4$ K ($T_{\mathrm{SR1}}$ and $T_{\mathrm{SR2}}$ are the starting and ending temperatures of SRT), the magnetization along the $a$-axis declines to zero, while that along the $c$-axis climbs to 2.77 emu/g synchronously. The magnetization along the $b$-axis remained negligible throughout the test temperature range. Therefore, the net moment rotates from the $a$- to $c$-axis, and correspondingly, the spin configuration of HEOR changes from $\Gamma_2$ ($F_x$, $C_y$, $G_z$) state to $\Gamma_4$ ($G_x$, $A_y$, $F_z$). This is consistent with the parent phase $YbFeO_3$ [15], $TmFeO_3$ [33], and $NdFeO_3$ [21], but inconsistent with going to $DyFeO_3$ [18], due to the different electron arrangements of the various $RE$ ions, which are the effect of the interactions between $RE$-4$f$ and Fe-3$d$ electrons. Besides, the magnitude of magnetization is generally unchanged before and after the SRT in the $RE$$FeO_3$ family. However, the magnetization of 1.86 emu/g at $T_{\mathrm{SR1}}$ is much smaller than that of 2.77 emu/g at $T_{\mathrm{SR2}}$ in HEOR, due to the rearrangement of $RE$ sublattices moment (from antiparallel to parallel coupling with Fe ions). The flip occurs in the SRT, resulting in the change of the net moment. A similar phenomenon was reported in $TmFeO_3$ [33], in which the SRT depends strongly on the 4$f$ electrons magnetic anisotropy and an AFM state of Tm moment is observed below $T_{\mathrm{SR1}}$.

The shifting trend of magnetization with temperature in the FCC mode between 2 K and 11 K is opposite to the $M$–$T$ curves in the ZFC and FCW modes along the $a$-axis. As the temperature declines, the magnetization

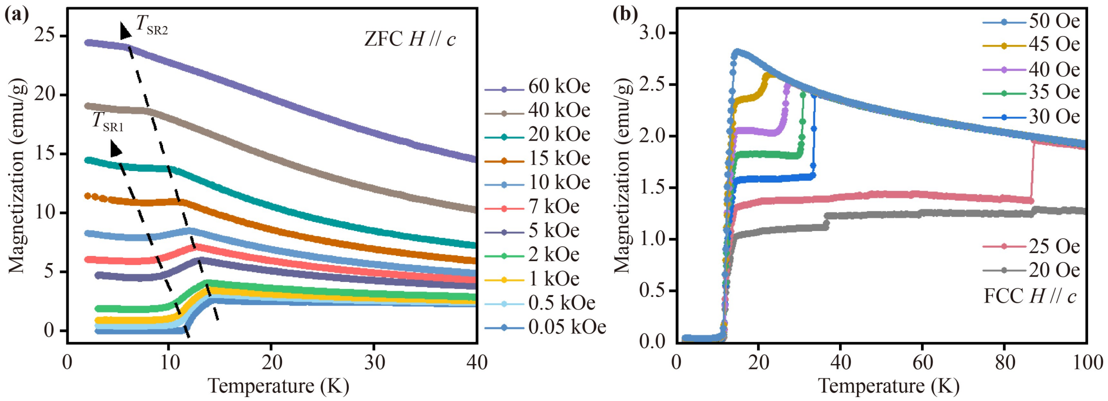

**Fig. 4** **(a, b)** Temperature dependences of magnetizations along the $c$-axis under various applied magnetic fields in ZFC and FCC modes, respectively. Arrows in (a) indicate the shifts of $T_{SR1}$ and $T_{SR2}$.

progressively rises until it reaches a peak at 2.7 K, after which it gradually falls. The opposite trend in the heating and cooling process along the same crystal axis has been found in $DyFeO_3$ [18]. Similarly, in HEOR, influenced by the Fe sublattice molecular field, some *RE* sublattices align their moments parallel to Fe during the cooling process until *RE* sublattices undergo an AFM transition at $T_{N2} = 2.7$ K, and then the magnetization lowers. Some *RE* sublattices' moments are antiparallel to that of Fe sublattices in ZFC and FCW modes, resulting in a decrease in magnetization. As temperature increases, the interactions between *RE* sublattices weaken, and that between Fe sublattices strengthen, resulting in the increasing of magnetization.

As shown in Fig. 4(a), we subsequently investigated the $M$–$T$ curves in ZFC mode under varied applied magnetic fields along the $c$-axis. The temperature dependence of magnetic field ($H$–$T$) phase diagram obtained from $M$–$T$ curves clearly emphasizes the magnetic behavior, as shown in Fig. 5. With an increasing of magnetic field, $T_{SR1}$ and $T_{SR2}$ are lowering and the temperature region broadens, demonstrating that SRT can be induced not only by temperature but also by a magnetic field. At 50 Oe, the net moment in $c$-axis is negligible when $T < T_{SR1}$, indicating that the Fe sublattice is completely in the $\Gamma_2$ state. The initial magnetization strength increases with the applied magnetic field, indicating that the SRT is gradually suppressed with the magnetic field, and a part of the net moment of the Fe sublattice is in the $c$-axis at $T < T_{SR1}$, leading to an incomplete antiferromagnetic state in the $c$-axis, and that the spin configuration is not a complete $\Gamma_2$ state either. Whereas, for magnetic fields up to 40000 Oe and above, the $\Gamma_2$ state of the Fe sublattice has disappeared and only the $\Gamma_{24}$ to $\Gamma_4$ transition exists. Compared to other orthoferrites in the $R\mathrm{FeO}_3$ system, the SRT modulation range of HEOR is an order of magnitude larger, which suggests that it is promising for applications in high-field magnetic sensing.

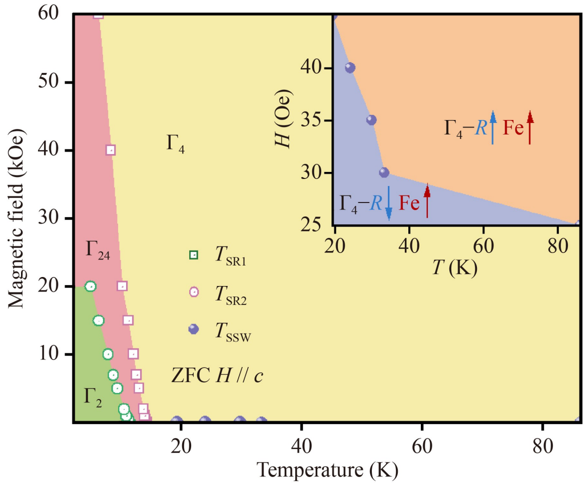

**Fig. 5** The $H$–$T$ magnetic phase diagram of HEOR single crystal. The illustration is a low-field phase diagram.

When it turns to low magnetic fields in FCC mode, there are interesting SSW effects as shown in Fig. 4(b). SSW effect does not occur at 20 Oe, because the system is in a metastable state. When the magnetic field reaches 25 Oe, the typical type-II SSW effect occurs at 86.4 K. Due to the interactions between *RE*-4$f$ and Fe-3$d$ electrons, *RE* sublattices spin flip from parallel to antiparallel with Fe sublattices and magnetization drops from 2.0 to 1.4 emu/g. A similar phenomenon is reported in $DyFeO_3$ [18]. The typical SSW effect turns to the continuous spin-switching (CSSW) effect from 30 Oe. When the D–M interaction between *RE* and Fe sublattices is greater than the influence of the applied field, the net moment of *RE* ions will reverse and result in the SSW effect. It still causes a change in magnetization to reach a lower energy stable state, but a continuous jump rather than a sudden change of the typical SSW effect. Increasing the applied magnetic field from 30 to 45 Oe, the temperature that the CSSW effect occurs ($T_{CSSW}$) decreases as shown in the inset of Fig. 5, so the

CSSW effect can be modulated by applied magnetic fields. As to 50 Oe, the SSW effect occurs in the SRT process as mentioned above, so there is no jump on the $M$–$T$ curve.

## 3.3 AC magnetic measurements

With measurements of AC susceptibility at various frequencies, the dynamic process of SRT in HEOR was systematically investigated. The oscillating component of magnetic field $H(t) = H_{\mathrm{AC}}\cos\omega t$ is applied, hence, the magnetization has the oscillating component $M(t) = M_{\mathrm{AC}}\cos(\omega t+\varphi)$. And the susceptibility is defined as

$$\chi_{\mathrm{AC}} = M_{\mathrm{AC}}/H_{\mathrm{AC}} = \chi' - \mathrm{i}\chi'', \tag{5}$$

where χ' denotes the real component correlated with the fluctuation in sample magnetization, and χ'' refers to the imaginary component and represents the absorption of the applied alternating magnetic field energy. We applied an AC magnetic field of 1 Oe along the $c$-axis without a DC magnetic field. $\chi'$–$T$ and $\chi''$–$T$ curves are shown in Figs. 6(a) and (d). χ' and χ'' show no frequency dispersion below $T_{\mathrm{SR1}}$ and above $T_{\mathrm{SR2}}$, indicating that the spin relaxation time ($\tau$) is too short to be observed. At various frequencies, a peak appears at around $T_{\mathrm{SR1}}$ of 11.7 K [see Fig. 6(b)] because the configuration of Fe sublattice changes from $\Gamma_2$ to $\Gamma_{24}$, and a step appears at around $T_{\mathrm{SR2}}$ of 14.2 K [see Fig. 6(c)], corresponding to the transition from $\Gamma_{24}$ to $\Gamma_4$. The phenomenon indicates two-step dynamic processes of Fe sublattices spin rotating from the $a$- to $c$-axis. A similar phenomenon has been reported in $\mathrm{ErFeO_3}$ [34], $\mathrm{TmFeO_3}$ [35], and $\mathrm{NdFeO_3}$ [36], but the change in those orthoferrites is irregular and unstable. The larger configurational entropy of HEOR makes the Gibbs free energy lower. The design of HEOR can stabilize the structure and make the dynamic process clearer. As the increase of frequency, the position of the peak and step of χ' remain unchanged. The independence shows the long-range order of HEOR. However, the peak value decreases with increasing frequency as shown in Fig. 6(b), because of the decrease in order degree. In Figs. 6(d) and (e), the position of the peak of χ'' also remains unchanged but the value is not monotonically decreasing. As the test frequency increases, it first increases and then decreases. The peak at 333 Hz indicates the greatest magnetic energy absorption.

## 3.4 Magnetocaloric effect

Calculate $\Delta S_{\mathrm{m}}$ of the $a$-, $b$-, and $c$-axes according to Maxwell's equations:

$$\Delta S_{\mathrm{m}} = \int_0^H \frac{\partial M}{\partial T}\mathrm{d}H. \tag{6}$$

Since the magnetization measurement is performed between discrete fields and temperatures, the $\Delta S_{\mathrm{m}}$ is calculated numerically by means of the expression:

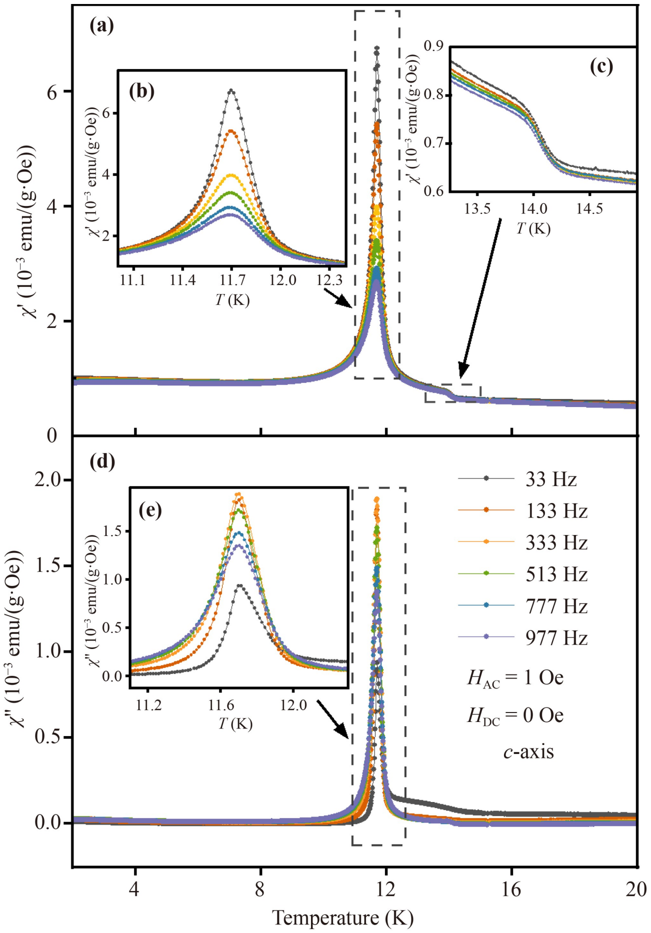

**Fig. 6** **(a, d)** Temperature dependences of the real and imaginary parts of AC susceptibility along the $c$-axis, respectively. $H_{\mathrm{AC}}$ = 1 Oe and $H_{\mathrm{DC}}$ = 0 Oe. **(b)** The enlarged plot of the peak in (a). **(c)** The enlarged plot of the step in (a). **(e)** The enlarged plot of the peak in (d).

$$\Delta S_{\mathrm{m}} = \sum\nolimits_i \frac{M_{i+1} - M_i}{T_{i+1} - T_i}\Delta H_i, \tag{7}$$

where $M_i$ and $M_{i+1}$ are the magnetic moments at $T_i$ and $T_{i+1}$, respectively, and $\Delta H_i$ is the little variation in the magnetic field. The temperature dependences of the magnetic entropy changes are depicted in Figs. 7(a)–(c). At 7 K and 70 kOe, the maximum of $-\Delta S_{\mathrm{m}}$ in $a$-axis is 8.11 J/(kg·K), while that in $b$- and $c$-axes are 6.99 J/(kg·K) and 2.32 J/(kg·K), respectively. The difference between $a$- and $c$-axes gets a maximum of 7.11 J/(kg·K) at 7 K and 50 kOe. The magnetic entropy values for the $a$- and $b$-axes are much larger than that for the $c$-axis, indicating that HEOR is easily magnetized in the $ab$ plane. The refrigeration capacity ($RC$) is calculated to determine its anisotropy, as shown in Fig. 7(d). Using such a magnetic anisotropy for refrigeration instead of traditional methods eliminates the mechanical loss of repeating the cold end and the heat dissipation

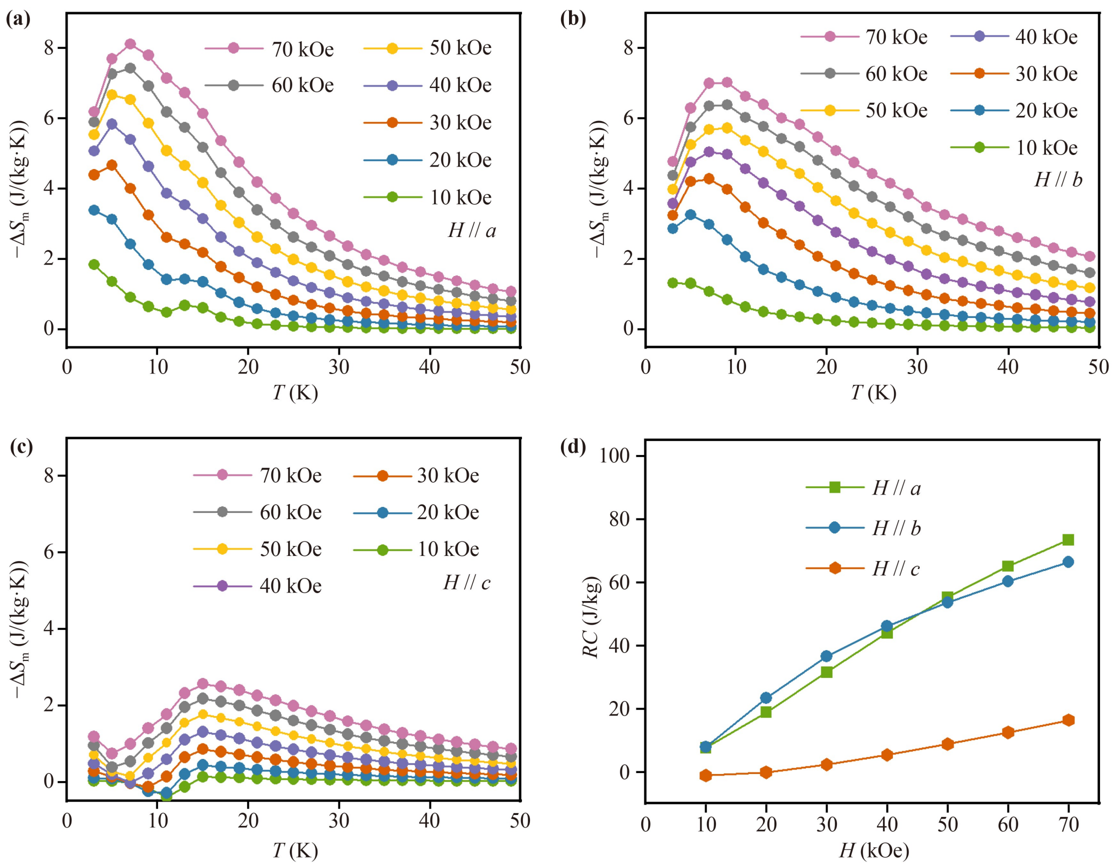

**Fig. 7** **(a–c)** Temperature dependences of the negative magnetic entropy change curves calculated from isothermal magnetic curves data along the *a*-, *b*-, and *c*-axes, respectively. **(d)** Magnetic field dependences of *RC* curves for the *a*-, *b*-, and *c*-axes.

end. Using the magnetic refrigeration formula (8) to calculate the magnetic refrigeration capacity ($RC$) of the three crystal axes,

$$RC = -\int_{T_1}^{T_2} \Delta S(T)\mathrm{d}T, \tag{8}$$

where $T_1$ and $T_2$ are the lower and higher temperatures at half the maximum of the entropy change [37]. As shown in Fig. 7(d), $RC$ reaches the maximum: 70.43 J/kg on the *a*-axis, 66.35 J/kg on the *b*-axis, and 16.27 J/kg on the *c*-axis at 70 kOe. Thus, the strong magnetic anisotropy makes HEOR an excellent refrigeration material.

## 4 Conclusion

In conclusion, we have grown the HEOR single crystal with high quality by the optical floating zone method and have studied its magnetic properties based on the high configurational entropy. Due to the rotation of the Fe ions moment, the SRT from $\Gamma_2$ to $\Gamma_4$ occurs, and it can be easily modulated by temperature and a broad applied magnetic field. Combined with the tunable SSW and CSSW, HEOR could be a potential material for magnetic sensing and/or spin switching applications. The AC susceptibility measurements identify the two-step SRT dynamic processes of $\Gamma_2$–$\Gamma_{24}$–$\Gamma_4$ and the long-range order. The magnetocaloric results show high anisotropy. At 50 kOe and 7 K, $-\Delta S_\mathrm{m}$ reaches 8.12 J/(kg·K) along *a*-axis but only 0.99 J/(kg·K) along *c*-axis. The large difference of $-\Delta S_\mathrm{m}$ in different crystallographic axes makes HEOR to be a good candidate for new magnetic refrigeration material at low temperatures.

**Declarations** The authors declare that they have no competing interests and there are no conflicts.

**Acknowledgements** This work was supported by the research grant from the National Natural Science Foundation of China (NSFC) (Nos. 12074242 and 12204298) and the Science and Technology Commission of Shanghai Municipality (No. 21JC1402600).

## Appendix A: Single crystal growth and structure characterization

The high-entropy orthoferrite HEOR polycrystalline samples were synthesized by the traditional solid-state reaction method with the ingredients $Tm_2O_3$, $Nd_2O_3$, $Dy_2O_3$, $Y_2O_3$, $Yb_2O_3$, and $Fe_2O_3$ of 99.99% purity. After precisely weighing by stoichiometric ratio and thoroughly grinding, raw materials were sintered at 1300 °C for 1000 min in the air using a box furnace (KSL-1700X). To achieve a sufficient chemical reaction, the sintered samples were adequately ground and pressed into tablets (thickness of 1.5 mm) at 10 MPa to narrow the gap between the powder particles for secondary sintering. Then crushed into powders and pressed into polycrystalline rods using an isostatic press (HP-M-SD-200) at 60 MPa. The optical floating zone furnace system with four halogen lamps (FZ-T-10000-H-VI-P-SH, Crystal System Inc.) was used to grow HEOR single crystal (using a polycrystalline rod as a seed crystal). The growth rate was 1.0 mm/h in the air atmosphere, the gas flow rate was 3.0 L/min, and the counter rotation speed was 20.0 rpm. Figure A1 shows the photograph of a high-quality HEOR single crystal, with a length of 54.0 mm and a diameter of 5.5 mm.

The high-resolution EDS mappings of *RE* and Fe elements are shown in Fig. A2, proving that the atomic ratio fits the definition of high-entropy oxide (HEO), with atomic fractions of Tm, Nd, Dy, Y, and Yb are 3.568%, 3.525%, 3.594%, 3.411%, and 3.411%, respectively, and the ratio of 1:0.99:1.01:0.96:0.96. The homogeneous distribution of *RE* ions in HEOR demonstrates the incorporation of various *RE* elements in the lattice structure. The atomic proportion of Fe is 18.393%, so the atomic ratio of *R* and Fe in HEOR is 1:1.05, which proves the concept of $RE$FeO$_3$ (that is, 1:1:3).

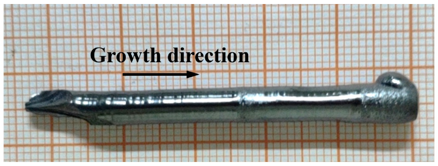

**Fig. A1** Picture of HEOR single crystal. The length is 54.0 mm and the diameter is 5.5 mm. The black arrow represents the direction of growth.

The lattice parameters $a$ = 5.3030 Å, $b$ = 5.5917 Å, and $c$ = 7.6310 Å are obtained from Rietveld refinement using FullProf Suite. Table 1 shows a comparison in lattice parameters and Fe–O bonding lengths to those of the parent crystal. Differences in Fe–O bond lengths are responsible for changes in the tilt of the Fe–$O_6$ octahedron. Different lattice constants indicate the distortion of crystal structure has changed and structure change is often the cause of the different properties.

## Appendix B: Magnetization characteristics

The *M*–*H* curves of HEOR along the *a*-, *b*-, and *c*-axes at 2 K were measured to verify the FM state, as shown in Fig. B1. The hysteresis only exists on the *a*-axis, while the magnetizations on the *b*- and *c*-axes fluctuate linearly with the applied magnetic field. So HEOR exhibits a weak FM state on the *a*-axis and AFM states on the *b*- and *c*-axes, corresponding to the $\Gamma_2$ ($F_x$, $C_y$, $G_z$) state. This is consistent with the *M*–*T* result that the sample is in $\Gamma_2$ state when the temperature is below

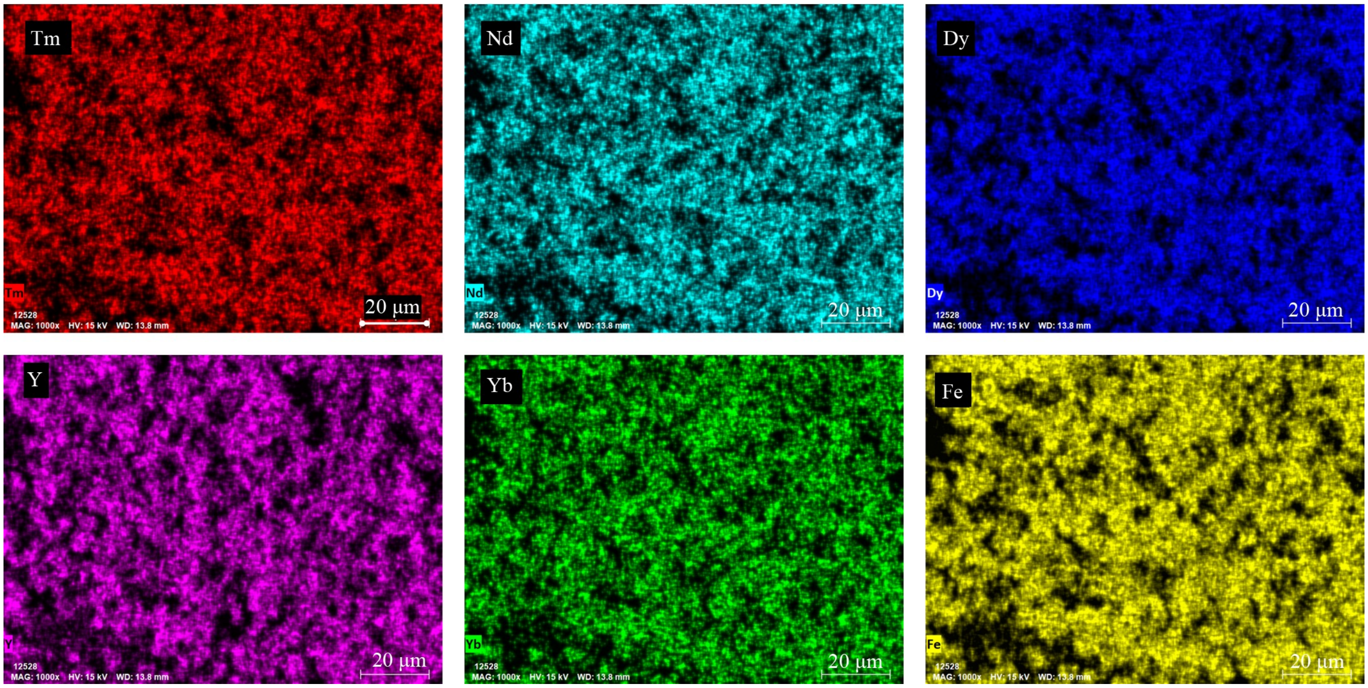

**Fig. A2** The SEM-EDS mapping of component elements Tm, Nd, Dy, Y, Yb, and Fe with a 20 μm scale bar, respectively.

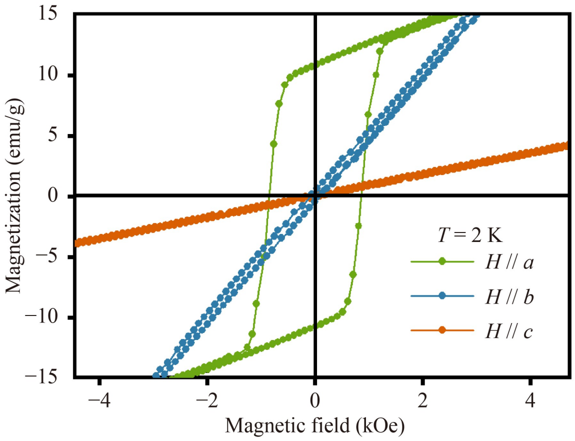

**Fig. B1** The applied magnetic field dependences of magnetization curves at 2 K.

$T_{\mathrm{SR1}} = 11.6$ K.

Figure B2 shows the isothermal magnetization curves of HEOR along three crystallographic axes at temperatures ranging from 2 K to 50 K with an interval of 2 K. The external magnetic field increases magnetization, but the trends are quite different along distinct crystallographic axes, indicating that the crystal has a strong anisotropy. $M$–$H$ curves from 10 to 14 K support the SRT. HEOR is weak ferromagnetic in the $a$-axis while antiferromagnetic in the $c$-axis at 10 K, and opposite at 14 K, showing that the SRT from $\Gamma_2$ ($F_x$, $C_y$, $G_z$) to $\Gamma_4$ ($G_x$, $A_y$, $F_z$) occurs.

The Arrott plots along the $a$-, $b$-, and $c$-axes, as shown in Figs. B2(d)–(f), are calculated from the isothermal magnetization curves. According to the Landau–Ginsburg mean field theory, free energy $F(M)$ can be expressed as

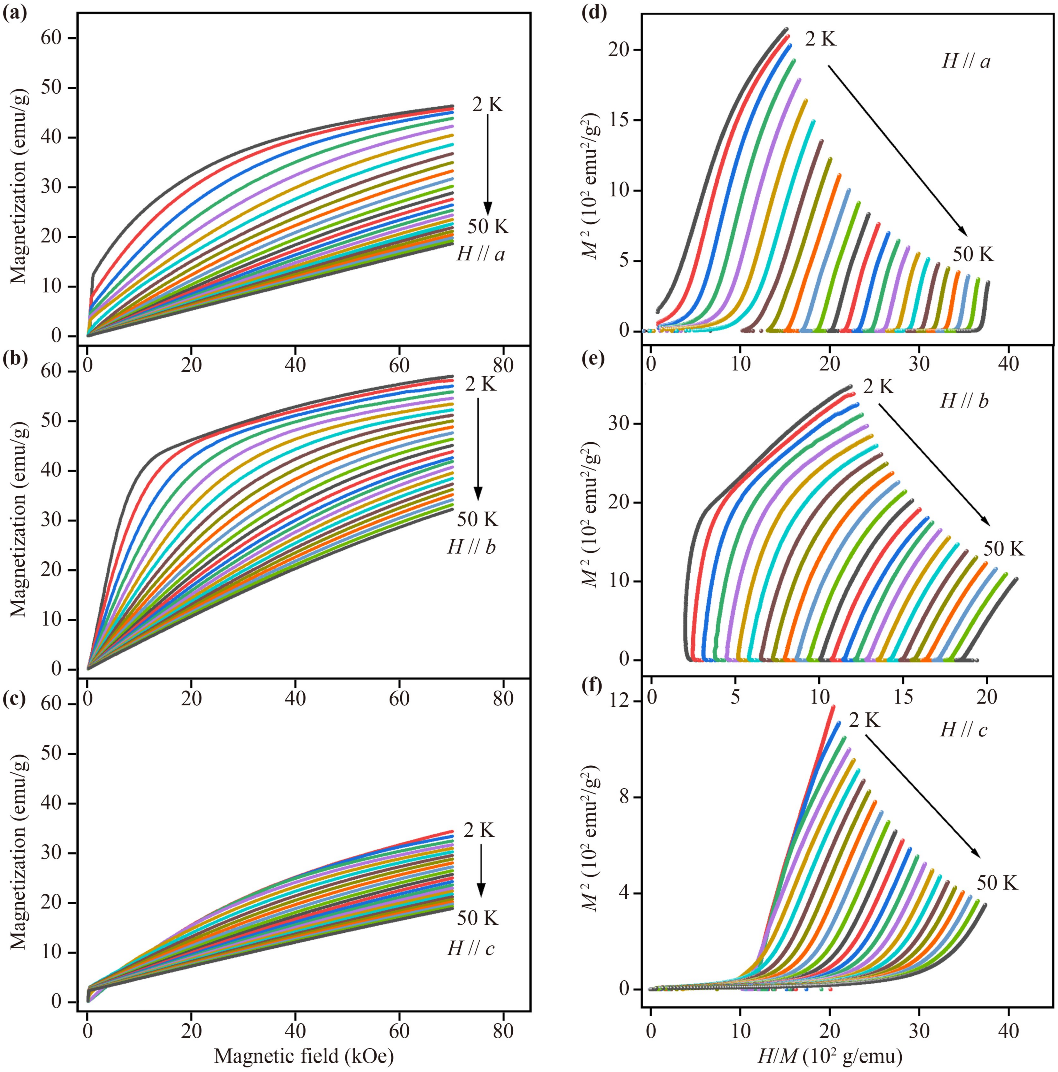

**Fig. B2** **(a–c)** Isothermal magnetic curves along the $a$-, $b$-, and $c$-axes at 2–50 K, $\Delta T = 2$ K. **(d–f)** The Arrott plots calculated from isothermal magnetic curves data for HEOR along the $a$-, $b$-, and $c$-axes.

$$F(M)=-HM+a_0\frac{T-T_c}{T_c}M^2+b_0M^4+\cdots. \tag{B1}$$

Taking the minimum of the free energy, and the following relation is obtained,

$$M^2=\frac{1}{4b_0}\frac{H}{M}-\frac{a_0}{2b_0}\frac{T-T_c}{T_c}, \tag{B2}$$

where $a_0$ and $b_0$ are constants. Hence, the slope of the $M^2$–$H/M$ curve is $1/(4b_0)$ [38]. According to Inoue and Shimizu's s–d model [39], the slope sign may be utilized to qualitatively identify the type of magnetic transition. In HEOR, the slopes are positive, indicating that the phase transitions are essentially second-order continuous along the crystal orientations.

## References

1. S. E. Hahn, A. A. Podlesnyak, G. Ehlers, G. E. Granroth, R. S. Fishman, A. I. Kolesnikov, E. Pomjakushina, and K. Conder, Inelastic neutron scattering studies of $YFeO_3$, *Phys. Rev. B* 89(1), 014420 (2014)
2. W. C. Fan, H. Y. Chen, G. Zhao, X. X. Ma, R. Chakaravarthy, B. J. Kang, W. L. Lu, W. Ren, J. C. Zhang, and S. X. Cao, Thermal control magnetic switching dominated by spin reorientation transition in Mn-doped $PrFeO_3$ single crystals, *Front. Phys.* 17(3), 33504 (2022)
3. R. L. White, Review of recent work on the magnetic and spectroscopic properties of the rare-earth orthoferrites, *J. Appl. Phys.* 40(3), 1061 (1969)
4. V. M. Goldschmidt, Die Gesetze der Krystallochemie, *Naturwissenschaften* 14(21), 477 (1926)
5. L. Shekhtman, O. Entin-Wohlman, and A. Aharony, Moriya's anisotropic superexchange interaction, frustration, and Dzyaloshinsky's weak ferromagnetism, *Phys. Rev. Lett.* 69(5), 836 (1992)
6. D. Treves, Magnetic studies of some orthoferrites, *Phys. Rev.* 125(6), 1843 (1962)
7. I. Dzyaloshinsky, A thermodynamic theory of "weak" ferromagnetism of antiferromagnetics, *J. Phys. Chem. Solids* 4(4), 241 (1958)
8. T. Yamaguchi and K. Tsushima, Magnetic symmetry of rare-earth orthochromites and orthoferrites, *Phys. Rev. B* 8(11), 5187 (1973)
9. E. F. Bertaut, Spin configurations of ionic structures: Theory and practice, in: Spin Arrangements and Crystal Structure, Domains, and Micromagnetics, edited by G. T. Rado and H. Suhl, Elsevier, 1963, page 149
10. D. Treves, Studies on orthoferrites at the Weizmann institute of science, *J. Appl. Phys.* 36(3), 1033 (1965)
11. T. Yamaguchi, Theory of spin reorientation in rare-earth orthochromites and orthoferrites, *J. Phys. Chem. Solids* 35(4), 479 (1974)
12. W. Y. Zhao, S. X. Cao, R. X. Huang, Y. M. Cao, K. Xu, B. J. Kang, J. C. Zhang, and W. Ren, Spin reorientation transition in dysprosium-samarium orthoferrite single crystals, *Phys. Rev. B* 91(10), 104425 (2015)
13. Ya. B. Bazaliy, L. T. Tsymbal, G. N. Kakazei, V. I. Kamenev, and P. E. Wigen, Measurements of spin reorientation in $YbFeO_3$ and comparison with modified mean-field theory, *Phys. Rev. B* 72(17), 174403 (2005)
14. X. Y. Zhao, K. L. Zhang, X. M. Liu, B. Wang, K. Xu, S. X. Cao, A. H. Wu, L. B. Su, and G. H. Ma, Spin reorientation transition in $Sm_{0.5}Tb_{0.5}FeO_3$ orthoferrite single crystal, *AIP Adv.* 6(1), 015201 (2016)
15. X. X. Ma, N. Yuan, X. Luo, Y. K. Chen, B. J. Kang, W. Ren, J. C. Zhang, and S. X. Cao, Field tunable spin switching in perovskite $YbFeO_3$ single crystal, *Mater. Today Commun.* 27, 102438 (2021)
16. J. S. Zhang, W. Y. Zhao, Z. J. Feng, J. Y. Ge, J. C. Zhang, and S. X. Cao, Spin reorientation and rare earth antiferromagnetic transition in single crystal $Sm_{0.15}Dy_{0.85}FeO_3$, *J. Alloys Compd.* 804, 396 (2019)
17. L. Hou, L. Shi, J. Y. Zhao, S. Y. Pan, Y. Xin, and X. Y. Yuan, Spin-reorientation transition driven by double exchange in $CeFeO_3$ ceramics, *J. Phys. Chem. C* 124(28), 15399 (2020)
18. S. X. Cao, L. Chen, W. Y. Zhao, K. Xu, G. H. Wang, Y. L. Yang, B. J. Kang, H. J. Zhao, P. Chen, A. Stroppa, R. H. Zheng, J. C. Zhang, W. Ren, J. Íñiguez, and L. Bellaiche, Tuning the weak ferromagnetic states in dysprosium orthoferrite, *Sci. Rep.* 6(1), 37529 (2016)
19. S. X. Cao, H. Z. Zhao, B. J. Kang, J. C. Zhang, and W. Ren, Temperature induced spin switching in $SmFeO_3$ single crystal, *Sci. Rep.* 4(1), 5960 (2014)
20. X. X. Zhang, Z. C. Xia, Y. J. Ke, X. Q. Zhang, Z. H. Cheng, Z. W. Ouyang, J. F. Wang, S. Huang, F. Yang, Y. J. Song, G. L. Xiao, H. Deng, and D. Q. Jiang, Magnetic behavior and complete high-field magnetic phase diagram of the orthoferrite $ErFeO_3$, *Phys. Rev. B* 100(5), 054418 (2019)
21. S. J. Yuan, W. Ren, F. Hong, Y. B. Wang, J. C. Zhang, L. Bellaiche, S. X. Cao, and G. Cao, Spin switching and magnetization reversal in single-crystal $NdFeO_3$, *Phys. Rev. B* 87(18), 184405 (2013)
22. M. Das, S. Roy, and P. Mandal, Giant reversible magnetocaloric effect in a multiferroic $GdFeO_3$ single crystal, *Phys. Rev. B* 96(17), 174405 (2017)
23. R. X. Huang, S. X. Cao, W. Ren, S. Zhan, B. J. Kang, and J. C. Zhang, Large rotating field entropy change in $ErFeO_3$ single crystal with angular distribution contribution, *Appl. Phys. Lett.* 103(16), 162412 (2013)
24. S. Mahana, U. Manju, and D. Topwal, Giant magnetocaloric effect in $GdAlO_3$ and a comparative study with $GdMnO_3$, *J. Phys. D Appl. Phys.* 50(3), 035002 (2017)
25. V. K. Pecharsky and Jr Gschneidner, Magnetocaloric effect and magnetic refrigeration, *J. Magn. Magn. Mater.* 200(1–3), 44 (1999)
26. M. J. Shao, S. X. Cao, S. J. Yuan, J. C. Shang, B. J. Kang, B. Lu, and J. C. Zhang, Large magnetocaloric effect induced by intrinsic structural transition in $Dy_{1-x}Ho_xMnO_3$, *Appl. Phys. Lett.* 100(22), 222404 (2012)
27. Y. J. Ke, X. Q. Zhang, H. Ge, Y. Ma, and Z. H. Cheng, Low field induced giant anisotropic magnetocaloric effect in $DyFeO_3$ single crystal, *Chin. Phys. B* 24(3), 037501 (2015)
28. J. W. Yeh, S. K. Chen, S. J. Lin, J. Y. Gan, T. S. Chin, T. T. Shun, C. H. Tsau, and S. Y. Chang, Nanostructured

high-entropy alloys with multiple principal elements: Novel alloy design concepts and outcomes, *Adv. Eng. Mater.* 6(5), 299 (2004)

29. C. M. Rost, E. Sachet, T. Borman, A. Moballegh, E. C. Dickey, D. Hou, J. L. Jones, S. Curtarolo, and J. P. Maria, Entropy-stabilized oxides, *Nat. Commun.* 6(1), 8485 (2015)
30. S. C. Jiang, T. Hu, J. Gild, N. X. Zhou, J. Nie, M. D. Qin, T. Harrington, K. Vecchio, and J. Luo, A new class of high-entropy perovskite oxides, *Scr. Mater.* 142, 116 (2018)
31. S. Y. Zhou, Y. P. Pu, Q. W. Zhang, R. K. Shi, X. Guo, W. Wang, J. M. Ji, T. C. Wei, and T. Ouyang, Microstructure and dielectric properties of high entropy $Ba(Zr_{0.2}Ti_{0.2}Sn_{0.2}Hf_{0.2}Me_{0.2})O_3$ perovskite oxides, *Ceram. Int.* 46(6), 7430 (2020)
32. A. Sarkar, B. Breitung, and H. Hahn, High entropy oxides: The role of entropy, enthalpy and synergy, *Scr. Mater.* 187, 43 (2020)
33. U. Staub, L. Rettig, E. M. Bothschafter, Y. W. Windsor, M. Ramakrishnan, S. R. V. Avula, J. Dreiser, C. Piamonteze, V. Scagnoli, S. Mukherjee, C. Niedermayer, M. Medarde, and E. Pomjakushina, Interplay of Fe and Tm moments through the spin-reorientation transition in $TmFeO_3$, *Phys. Rev. B* 96(17), 174408 (2017)
34. H. Shen, Z. X. Cheng, F. Hong, J. Y. Xu, S. J. Yuan, S. X. Cao, and X. L. Wang, Magnetic field induced discontinuous spin reorientation in $ErFeO_3$ single crystal, *Appl. Phys. Lett.* 103(19), 192404 (2013)
35. A. Bombik and A. W. Pacyna, AC susceptibility of $TmFeO_3$ single-crystal, *J. Magn. Magn. Mater.* 220(1), 18 (2000)
36. G. B. Song, J. J. Jiang, B. J. Kang, J. C. Zhang, Z. X. Cheng, G. H. Ma, and S. X. Cao, Spin reorientation transition process in single crystal $NdFeO_3$, *Solid State Commun.* 211, 47 (2015)
37. K. A. GschneidnerJr, V. K. Pecharsky, and A. O. Tsokol, Recent developments in magnetocaloric materials, *Rep. Prog. Phys.* 68(6), 1479 (2005)
38. A. Arrott, Criterion for ferromagnetism from observations of magnetic isotherms, *Phys. Rev.* 108(6), 1394 (1957)
39. J. Inoue and M. Shimizu, First- and second-order magnetic phase transitions in $(R\text{-}Y)Co_2$ and $R(Co\text{-}Al)_2$ ($R$ = heavy rare-earth element) compounds, *J. Phys. F Met. Phys.* 18(11), 2487 (1988)